

1 **Main:**

2 Severe acute respiratory syndrome coronavirus 2 (SARS-CoV-2) is a causative agent for the
3 COVID-19 pandemic that is disrupting human health and global economy. Although 80% of
4 COVID-19 patients display mild or no symptoms, 20% of them developed serious conditions
5 mostly in the population of elderly person and those with underlying pre-existing medical
6 conditions. The virus has caused more than two million deaths and more than 100 million cases
7 worldwide. Most deaths are associated with an acute respiratory distress syndrome (ARDS) and
8 tissue damage linked to virus-induced hyper-immune responses ¹.

9 SARS-CoV-2 and SARS-CoV-1 genomes encode a small envelope (E) protein that is a
10 critically important component in viral life cycle of assembly, release, and virulence ². SARS-CoV-
11 2 E is composed of 75 amino acid residues with two distinct domains: an N-terminal
12 transmembrane (TM) domain followed by a C-terminal domain. E is a multifunctional protein.
13 Besides its structural roles required to induce membrane curvature for viral assembly in
14 cooperation with the viral membrane (M) protein, E mediates host immune responses through two
15 distinct mechanisms: a pore-forming TM domain related to the activation of NLRP3-
16 inflammasome ³; and a PDZ (PSD-95/Dlg/ZO-1)-binding function via its C-terminal domain ^{4,5}.
17 Structurally, the TM domain of SARS-CoV-2 E forms a pentameric ion channel, similar to that of
18 SARS-CoV-1 E ^{6,7}. However, the C-terminal domain has no well-defined structure, perhaps due
19 to the lack of a stable complex.

20 In humans, there are about 150 unique proteins encoding one or more PDZ domains.
21 These PDZ domains contain 80-110 amino acid residues and are essential in regulating human
22 immune responses and numerous physiological and pathological activities ⁸. PDZ-domain-
23 containing proteins in cell junctions have been hijacked by various viruses to potentiate their
24 virulence ⁸. Both SARS-CoV-2 and SARS-CoV-1 E proteins harbor a PDZ-binding motif (PBM) at
25 their C-termini. Although the exact mechanism is unknown, interactions between the PBM and a
26 human cell junction protein, PALS1, showed that E causes the relocation of PALS1 from the cell
27 junction to the endoplasmic-reticulum–Golgi intermediate compartment (ERGIC) site where E is
28 localized and virus assembly and maturation occur ⁴. As a cell junction protein, PALS1 is a
29 structural component of an apical Crumbs (Crb) complex in the establishment and maintenance
30 of cell polarity and intercellular tight junctions ^{9,10}. In addition to PALS1, E also interacts to PDZ-
31 containing adhesion junction protein syntenin ⁵, tight junction protein ZO1 ¹¹ and other cell-junction
32 proteins ¹². The relocation of these cell-junction proteins in lung epithelial cells contributes to
33 vascular leakage, diffuse alveolar damage (DAD), cytokine storm initiation, and acute respiratory

1 distress syndrome (ARDS), commonly leading to death in elderly COVID-19 patients and those
2 with underlying conditions ².

3 The PBM in E contains four conserved residues (DLLV) and is conserved between SARS-
4 CoV-2 and SARS-CoV-1 viruses. The motif appears to play a critical role in virulence because
5 mutants without the PBM are either attenuated or nonviable ^{5,13}. Binding assays using the 10-
6 residue C-terminal peptides of SARS-CoV-2 E and SARS-CoV-1 E show enhanced binding
7 affinity of SARS-CoV-2 E peptide to the PDZ domain in PALS1 ¹⁴. However, there is a lack of
8 structural information to define such protein-protein interactions, which hinders further
9 understanding of the mechanisms of the E-mediated virulence. In this work, we describe the
10 structure of the PALS1-E complex to define the mechanism of recognition of the PALS1 PDZ and
11 SH3 domains by the C-terminal PBM of the E protein.

12 **Results**

13 **Production of the PALS1-E complex**

14 PALS1 contains five domains, two N-terminal L27 domains and three C-terminal domains, PDZ,
15 SH3, and GK (named as PSG). To improve protein stability, we expressed and purified the PSG
16 (residues 236–675) without a loop between the SH3 and GK domains ⁹ (**Fig. S1a**). The expressed
17 protein was purified by Ni-NTA affinity resins followed by size-exclusion chromatography (SEC)
18 (**Fig. S1b**). Based on the SEC analysis, we found that majority of PSG is a dimer (**Fig. S1c**).

19 To study the structural basis for recognition of PALS1 PSG by SARS-CoV-2 E C-term
20 domain, we synthesized an E C-term 18-amino-acid peptide (Ec18) containing the PBM (**Fig. 1a**).
21 To check the binding affinity between Ec18 and PSG, we labeled PSG using a fluorescence dye
22 and titrated it using a serial dilution of Ec18. Using a microscale thermophoresis method ¹⁵, we
23 measured the K_d as 11.2 μM (**Fig. S1d**). Our measured value is consistent with the binding
24 affinity using a 10-aa peptide and the PDZ domain alone; where the measured K_d is 40 μM (Toto
25 et al., 2020). Considering the low affinity between Ec18 and PSG, we used a high ratio of Ec18
26 for complex formation by incubating purified PSG with Ec18 at a molar ratio of 1:10 for 2hrs at
27 room temperature.

28 **Structure determination**

29 We subjected the PSG-Ec18 complex to analysis using single-particle Cryo-EM. Our initial 2D
30 class averages showed a preferred particle orientation. To get additional views of the complex,
31 we performed detergent screening and found that the inclusion of 0.05% CHAPS allowed PSG-
32 Ec18 particles to distribute evenly (**Fig. 1a**) and helped us obtain multiple views after 2D class
33 averaging (**Fig. 1b, 1e**). We optimized our particle picking procedure using a local dynamic mask

1 for defocus-based particle picking ¹⁶. After iterative 2D and 3D classifications and refinements
2 with per-particle CTF and Bayesian polishing (**Fig. S2**) with Relion3 and CryoSPARC ^{17,18}, we
3 obtained a final reconstruction at 3.65 Å (**Fig. 1c**) using Fourier Shell Correlation of 0.143 as a
4 cutoff (**Fig. 1d**). The map shows clear secondary structures and side chains that allowed us to
5 build and refine atomic models (**Fig. S3**).

6 **Structure of the PSG-Ec18 complex**

7 The solved structure contains a dimer of PSG and a single Ec18 (**Fig. 2a**). In one PSG monomer,
8 the PDZ, SH3, and GK domains were observed; while in the other monomer, the PDZ domain
9 was missing. However, in our initial 3D classification, we observed a class with a highly disordered
10 region corresponding to the missing PDZ domain (**Fig. S2**). In comparison to the crystal structure
11 of the PSG dimer in complex with its physiological ligand Crb-CT ⁹, the PDZ and SH3 domains
12 are rotated about 38° relative to the GK domain in the PSG-Ec18 complex (**Fig. S4a**).

13 In our structure, Ec18 is inserted in a hydrophobic pocket between the PDZ and SH3
14 domains through the PBM(72DLLV75) (**Fig. 2b, c**). The density coverage for residues Leu74-
15 Val75 on the Ec18 and Phe318 on the PDZ domain are well defined and help position Ec18 in
16 the binding pocket. Residues Phe318, Leu321, Leu267, Pro266, and Val284 from PDZ and
17 Leu369 and Leu403 from SH3 are involved in forming the hydrophobic binding pocket. Phe318,
18 Leu369, and Leu403 in PALS1 and Leu74 and Val75 in Ec18 have side-chain densities,
19 consistent with roles in the formation and recognition of the binding pocket, respectively. Among
20 these residues, Phe318 is sandwiched by two hydrophobic residues Leu73 and Val75 in Ec18,
21 representing another notable recognition feature.

22 There are two SH3 and two GK domains in the structure. The overall structure for the GK
23 and SH3 domains are similar: the root mean square deviation (RMSD) is 1.18 Å for 205 C_α atoms
24 in the GK domain and 1.23 Å for 65 C_α atoms in the SH3 domain. Nevertheless, we found
25 conformational changes for two SH3 loops associated with Ec18 binding (**Fig. 2d**). One loop
26 containing residue Leu403 moved as much as 4.5 Å; and the other loop containing Leu369 also
27 moved so that Leu369 has a closer engagement with Leu74 from Ec18. We thus propose that
28 residues Leu369 and Leu403 from the SH3 domain further stabilize Ec18 binding to the PDZ
29 domain.

30 **Discussion**

31 Many viruses have developed strategies to hijack human PDZ-domain containing proteins to
32 increase their virulence and evade immune responses ^{19,20}. The structure of the PSG-Ec18
33

1 complex allows us to explain the SARS-CoV-2 E-mediated PALS1 relocation and vascular
2 damage.

3 PALS1 is an integral part of an apical cell polarity complex consisting of Crumbs, PALS1,
4 and PATJ¹⁰. Under physiological conditions, PALS1 interacts with the Crumbs C-terminus (Crb-
5 CT) through the PSG module⁹ and interacts with PATJ through its N-term L27 domain²¹ (**Fig.**
6 **3a**). In SARS-CoV-2 infected lung epithelial cells, the replication and transcription of the virion
7 genome produce a high load of the E protein which localizes to the ERGIC region for viral
8 assembly and budding²². The specific interactions between Ec18 and PALS1 PDZ/SH3 recruit
9 PALS1 to the site of virus assembly and disrupt the polarity complex and vascular structure⁴.
10 Although the affinity between E and PALS1 is at a μM range (**Fig. S1d**)¹⁴, the viral E can have a
11 high local concentration and competes dynamically with its physiological ligand of Crumbs and
12 pulls PALS1 out from the intercellular junction space (**Fig. 3b**). Consequently, the inter-epithelial
13 junctions loosen and leak. The leaking junctions promote local viral spreading, flow of fluid and
14 multiple types of immune cells (such as monocytes and neutrophils) into lung alveolar spaces,
15 causing lung damage, and cytokine storm (**Fig. 3b**) that eventually leads to ARDS, a causative
16 factor that contributes to the severity of symptoms and deaths in a subset of COVID-19 patients.

17 Virus-host interactions have been proposed to potentiate viral fitness and virulence²³.
18 Mutation in viruses, including SARS-CoV-2, that convey a selective advantage with respect to
19 replication, assembly, release and spreading can accelerate the viral life cycle. In this work, we
20 provide the first structure to show interactions between the SARS-CoV-2 E protein and human
21 PALS1. The complex structure provides an atomic basis to explain E-mediated virulence through
22 its C-terminal PBM¹³. Interestingly, when the C-term PBM was deleted in SARS-CoV variants,
23 the PBM was recovered from passage in the host, clearly demonstrating its involvement in viral
24 fitness and virulence. In addition to E, SARS-CoV-2 and SARS-CoV-1 encode another PBM-
25 containing protein ORF3a, which could both be involved in the recruitment of PDZ-containing
26 proteins for viral fitness and virulence²⁴.

27 The interaction between Ec18 and PALS1 is much weaker than the interaction between
28 PALS1 and its physiological ligand Crb-CT⁹. Based on the alignment of PSG-Ec18 and PSG-
29 Crb-CT structures (**Fig. S4b**), the terminal isoleucine in Crb-CT is inserted deeply in the PDZ
30 pocket. So, a peptide inhibitor with a C-terminal isoleucine, leucine, or even phenylalanine may
31 penetrate the pocket deeper and with a higher affinity. In addition, an arginine in Crb-CT PBM
32 interacts with Phe318 unfavorably; changing this residue to a hydrophobic residue such as leucine
33 or phenylalanine may enhance its hydrophobic interactions with Phe318. Interestingly, through
34 mutations in hosts, SARS-CoV-2 variants have acquired a number of mutations in the PBM

(72DLLV75) for viral fitness and virulence. Notable PBM mutations are D72Y, D72H, L73F, V75L, V75F^{25,26}. We hence propose that a hybrid peptide containing Crb-CT and viral PBM mutations could weaken the PALS1-E interactions to suppress E-mediated lung damage and virulence.

References

- 1 Mehta, P. *et al.* COVID-19: consider cytokine storm syndromes and immunosuppression. *Lancet (London, England)* **395**, 1033-1034, (2020).
- 2 Schoeman, D. & Fielding, B. C. Is there a link between the pathogenic human coronavirus envelope protein and immunopathology? A review of the literature. *Frontiers in Microbiology* **11**, 2086, (2020).
- 3 Nieto-Torres, J. L. *et al.* Severe acute respiratory syndrome coronavirus E protein transports calcium ions and activates the NLRP3 inflammasome. *Virology* **485**, 330-339, (2015).
- 4 Teoh, K.-T. *et al.* The SARS Coronavirus E Protein Interacts with PALS1 and Alters Tight Junction Formation and Epithelial Morphogenesis. *Molecular Biology of the Cell* **21**, 3838-3852, (2010).
- 5 Jimenez-Guardeño, J. M. *et al.* The PDZ-Binding Motif of Severe Acute Respiratory Syndrome Coronavirus Envelope Protein Is a Determinant of Viral Pathogenesis. *PLoS Pathogens* **10**, e1004320, (2014).
- 6 Schoeman, D. & Fielding, B. C. Coronavirus envelope protein: current knowledge. *Virology Journal* **16**, 69, (2019).
- 7 Mandala, V. S. *et al.* Structure and drug binding of the SARS-CoV-2 envelope protein transmembrane domain in lipid bilayers. *Nature Structural & Molecular Biology* **27**, 1202-1208, (2020).
- 8 Christensen, N. R. *et al.* PDZ domains as drug targets. *Advanced Therapeutics* **2**, 1800143, (2019).
- 9 Li, Y. J. *et al.* Structure of Crumbs tail in complex with the PALS1 PDZ-SH3-GK tandem reveals a highly specific assembly mechanism for the apical Crumbs complex. *Proceedings of the National Academy of Sciences of the United States of America* **111**, 17444-17449, (2014).
- 10 Wells, C. D. *et al.* A Rich1/Amot complex regulates the Cdc42 GTPase and apical-polarity proteins in epithelial cells. *Cell* **125**, 535-548, (2006).
- 11 Shepley-McTaggart, A. *et al.* SARS-CoV-2 Envelope (E) Protein Interacts with PDZ-Domain-2 of Host Tight Junction Protein ZO1. *bioRxiv*, 10.1101/2020.1112.1122.422708, (2020).
- 12 Caillet-Saguy, C. *et al.* Host PDZ-containing proteins targeted by SARS-Cov-2. *bioRxiv*, 10.1101/2021.1102.1101.429176 (2021).
- 13 Castaño-Rodríguez, C. *et al.* Role of Severe Acute Respiratory Syndrome Coronavirus Viroporins E, 3a, and 8a in Replication and Pathogenesis. *mBio* **9**, e02325-02317, (2018).
- 14 Toto, A. *et al.* Comparing the binding properties of peptides mimicking the Envelope protein of SARS-CoV and SARS-CoV-2 to the PDZ domain of the tight junction-associated PALS1 protein. *Protein Science* **29**, 2038–2042, (2020).
- 15 Jerabek-Willemsen, M., Wienken, C. J., Braun, D., Baaske, P. & Duhr, S. Molecular interaction studies using microscale thermophoresis. *Assay and drug development technologies* **9**, 342-353, (2011).
- 16 McSweeney, D. M., McSweeney, S. M. & Liu, Q. A self-supervised workflow for particle picking in cryo-EM. *Iucrj* **7**, 719-727, (2020).

- 1 17 Zivanov, J. *et al.* New tools for automated high-resolution cryo-EM structure determination
2 in RELION-3. *Elife* **7**, e42166, (2018).
- 3 18 Punjani, A., Zhang, H. & Fleet, D. J. Non-uniform refinement: adaptive regularization
4 improves single-particle cryo-EM reconstruction. *Nature Methods* **17**, 1214-1221, (2020).
- 5 19 Gutierrez-Gonzalez, L. H. & Santos-Mendoza, T. Viral targeting of PDZ polarity proteins
6 in the immune system as a potential evasion mechanism. *Faseb J* **33**, 10607-10617,
7 (2019).
- 8 20 James, C. D. & Roberts, S. Viral interactions with PDZ domain-containing proteins—an
9 oncogenic trait? *Pathogens* **5**, 8. <https://doi.org/10.3390/pathogens5010008> (2016).
- 10 21 Roh, M. H. *et al.* The Maguk protein, Pals1, functions as an adapter, linking mammalian
11 homologues of Crumbs and Discs Lost. *J Cell Biol* **157**, 161-172, (2002).
- 12 22 Wong, N. A. & Saier, M. H. The SARS-Coronavirus Infection Cycle: A Survey of Viral
13 Membrane Proteins, Their Functional Interactions and Pathogenesis. *International Journal*
14 *of Molecular Sciences* **22**, 1308, (2021).
- 15 23 Lim, Y. X., Ng, Y. L., Tam, J. P. & Liu, D. X. Human coronaviruses: a review of virus–host
16 Interactions. *Diseases* **4**, 26. [10.3390/diseases4030026](https://doi.org/10.3390/diseases4030026), (2016).
- 17 24 Jimenez-Guardeño, J. M. *et al.* Identification of the mechanisms causing reversion to
18 virulence in an attenuated SARS-CoV for the design of a genetically stable vaccine. *PLoS*
19 *Pathogens* **11**, e1005215, (2015).
- 20 25 Hassan, S. S., Choudhury, P. P. & Roy, B. Molecular phylogeny and missense mutations
21 at envelope proteins across coronaviruses. *Genomics* **112**, 4993-5004, (2020).
- 22 26 Rahman, M. S. *et al.* Mutational insights into the envelope protein of SARS-CoV-2. *Gene*
23 *reports* **22**, 100997, (2021).
- 24 27 Zheng, S. Q. *et al.* MotionCor2: anisotropic correction of beam-induced motion for
25 improved cryo-electron microscopy. *Nature Methods* **14**, 331-332, (2017).
- 26 28 Zhang, K. Gctf: Real-time CTF determination and correction. *Journal of Structural Biology*
27 **193**, 1-12, (2016).
- 28 29 Vilas, J. *et al.* Local resolution estimates of cryoEM reconstructions. *Current Opinion in*
29 *Structural Biology* **64**, 74-78, (2020).
- 30 30 Adams, P. D. *et al.* PHENIX: a comprehensive Python-based system for macromolecular
31 structure solution. *Acta Crystallographica Section D: Biological Crystallography* **66**, 213-
32 221, (2010).
- 33 31 Casañal, A., Lohkamp, B. & Emsley, P. Current developments in Coot for macromolecular
34 model building of Electron Cryo-microscopy and Crystallographic Data. *Protein Science*
35 **29**, 1055-1064, (2020).
- 36 32 Williams, C. J. *et al.* MolProbity: More and better reference data for improved all-atom
37 structure validation. *Protein Science* **27**, 293-315, (2018).
- 38
39

40 **Acknowledgments** We thank Gongrui Guo for initial discussions on the project, LBMS staff for
41 the help with the Cryo-EM operation and data acquisition, and Computational Science Initiative
42 (CSI) for support on computation. This work was supported in part by Brookhaven National
43 Laboratory COVID-19 LDRD. LBMS is supported by the U.S. Department of Energy, Office of
44 Science, Office of Biological and Environmental Research. Atomic coordinates and experimental
45 map have been deposited in the RCSB Protein Data Bank (PDB) under the accession code XXXX.

1 **Author contributions** Q.L. designed the study and experiments. J.C., Y.C., C.P., L.W. and Q.L.
2 performed the experiments. J.C., S.M., J.S., and Q.L. analyzed the data. Q.L. wrote the
3 manuscript with help from the other coauthors.

4 **Competing interests** Authors declare no competing interests.

5
6 **Figure Captions**

7 **Figure 1. Structure determination by single-particle Cryo-EM.** (a) A typical motion-corrected
8 Cryo-EM micrograph. (b) 2D class averages. (c) Reconstructed map colored with local resolutions.
9 (d) Fourier Shell Correlation (FSC) curve for the 3D reconstruction to determine the structure
10 resolution. (e) Orientation distribution for particles used in 3D reconstruction.

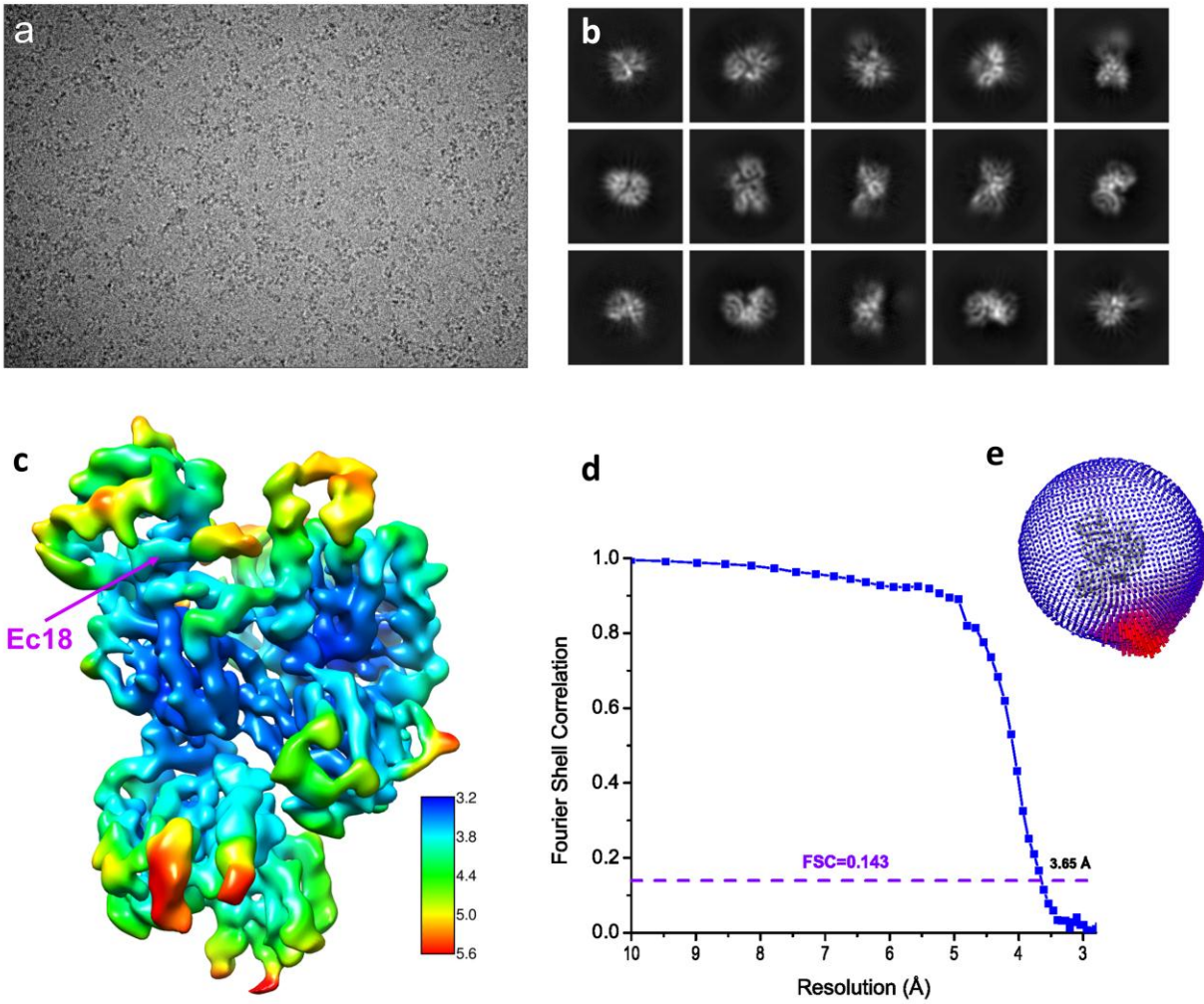
11 **Figure 2. Recognition of the PALS1 PDZ and SH3 domains by the E PBM.** (a) Structure of
12 the PSG-Ec18 complex shown as cartoons with different colors for different domains. Ec18 is
13 shown as magenta sticks. (b) Binding site structure. Hydrophobic residues forming the binding
14 pocket were shown as sticks. Potential density map for the binding site is shown as gray
15 isomeshes contoured at 5.5σ . (c) Surface representation of the binding site with Ec18 showing as
16 sticks. (d) Superimposition of the two PSG monomers to show conformational changes in SH3
17 domains. The PDZ domain in the second monomer is disordered.

18 **Figure 3. A proposed model of the E-mediated PALS1 relocalization and vascular damage.**
19 (a) A schematic drawing of two adjacent lung epithelial cells with the Crumbs apical complex
20 maintaining cell polarity and tight junction formation. (b) SARS-CoV-2 E protein interacts with
21 PALS1 and recruits it to the ERGIC site, causing vascular leakage and damage to cell junctions,
22 promoting viral spreading and cytokine storm, and leading to ARDS and in some cases deaths.

1

2

Fig. 1

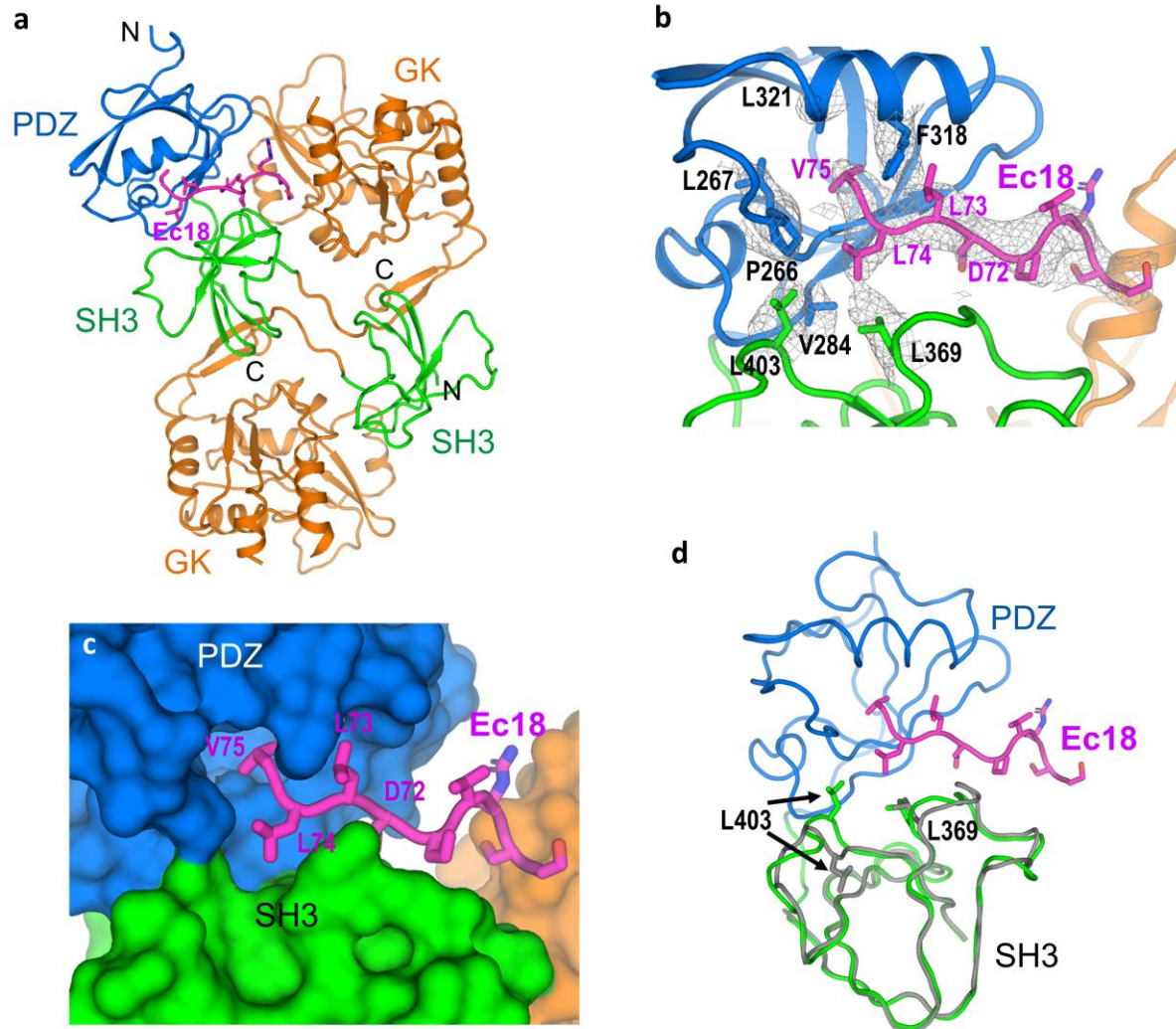


3

1

2

Fig. 2

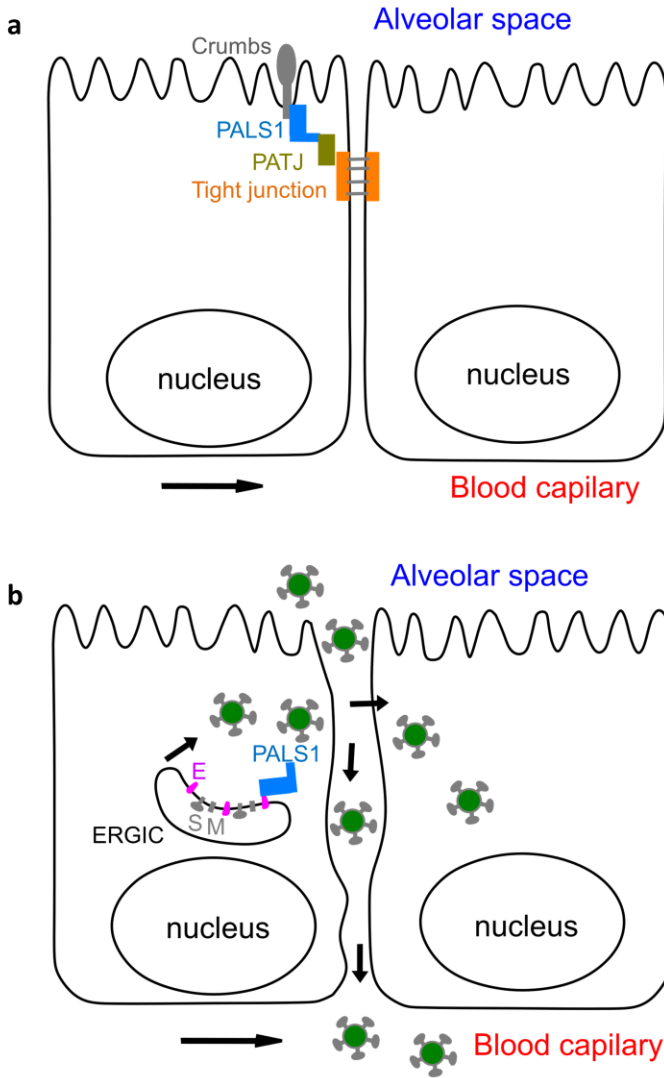


3

4

1

Fig. 3



2

1 **Methods**

2 **Protein expression and purification**

3 The gene encoding PASL1-PSG domains (residues 236–675) with a deletion between 411-460
4 was codon optimized for bacterial expression and synthesized by Genscript (www.genscript.com)
5 and cloned into pET16-b with an N-terminal 10x his tag followed by a TEV cleavage site.

6 The protein was overexpressed in *Escherichia coli* BL21 (DE3) pLysS at 16°C for 18 hrs
7 induced by addition of 0.4 mM IPTG (final) to the cell culture with an A600 of 1.0. Harvested cells
8 were resuspended in extraction buffer containing 30 mM Tris, pH 7.5, 150 mM NaCl, 1.0 mM
9 TCEP, 0.2 mM PMSF. Cells were lysed using an EmulsiFlex-C3 Homogenizer (Avestin, Ottawa,
10 Canada). After centrifugation at 26,000xg for 30 mins, the supernatant was collected for affinity
11 purification by nickel-nitrilotriacetic acid affinity chromatography (Ni-NTA, Superflow, Qiagen).
12 The eluate was concentrated and buffer exchanged for tag removal by incubation with TEV
13 protease overnight at 4 °C. The protein-containing solution was passed through Ni-NTA resin
14 again to remove the cleaved tag and the protein flow-through fractions were collected,
15 concentrated and applied to a size-exclusion column (TSKgel G3000SW column, Tosoh
16 Bioscience) pre-equilibrated with 25 mM Tris, pH 7.5, 100 mM NaCl, 1 mM TCEP. Highly enriched
17 protein was concentrated to about 10 mg/ml using an Amicon Ultra-15 centrifugal filter with a
18 molecular cutoff of 30 kDa (Milipore, Inc).

19 **Cryo-EM sample preparation and data collection**

20 To make the PSG-Ec18 complex, we mixed PSG and Ec18 at a molar ratio of 1:10 at a final
21 concentration of 2 mg/ml. After incubation for 2 hrs at room temperature, we added 0.05% CHAPS
22 (3-((3-cholamidopropyl) dimethylammonio)-1-propanesulfonate) to the sample immediately
23 before applying 3 µl of the sample to a glow-discharged QuanFoil Au grid (0.6/1.0). Vitrification
24 was performed using a ThermoFisher Mark IV vitrobot with a blotting condition of 3.5 sec blot time,
25 0 blot force, and 100% humidity at 6 °C.

26 Cryo-EM data were collected with the use of a ThermoFisher Titan Krios (G3i) equipped
27 with a Gatan K3 camera and a BioQuantum energy filter. With a physical pixel size of 0.684 Å, a
28 total dose of 64 e⁻/Å² were fractioned to 52 frames under the super-resolution mode using the
29 ThermoFisher data acquisition program EPU. A total of 12,861 movies were collected with an
30 energy filter width of 20 eV throughout the data acquisition. Data collection statistics is listed in

31 **Table S1.**

32 **Cryo-EM data analysis**

1 Beam-induced motion correction was performed using MotionCorr2 ²⁷ through a wrapper in
2 Relion3 ¹⁷ with a bin-factor of 2. Corrected and averaged micrographs were further corrected by
3 CTF estimation using Gctf ²⁸. Micrographs with an estimated resolution lower than 4.5 Å were
4 discarded from further processing. Particle picking was performed using Localpicker ¹⁶ which uses
5 per-micrograph defocus values (estimated by Gctf) to set up picking parameters. We picked up a
6 total of 6,375,890 particles, extracted and binned them to 64 pixels with a pixel size of 2.736 Å.

7 We used CryoSPARC ¹⁸ and Relion3 for 2D and 3D class averages and 3D refinements.
8 Specifically, we used 2D class averaging for initial particle cleanup which resulted in 2,193,282
9 particles. Among these particles, we produced an initial 3D model using CryoSPARC and used
10 the model to perform 3D classifications in Relion3 for five classes with a pixel size of 2.736 Å (**Fig.**
11 **S2**). Particles from the 3D class with the best structural feature were selected. A total of 715,010
12 particles were selected, re-centered, and re-extracted at 256 pixels with a pixel size of 0.684 Å.

13 Extracted particles were further auto-refined to convergence with Relion3 followed by non-
14 alignment 3D classification into three classes (**Fig. S2**). Particles from the best class (7.2%) were
15 selected for CTF refinement and Bayesian polishing in Relion3 and non-uniform refinement in
16 CryoSPAC to reach a refined reconstruction at 3.65 Å resolution based on gold-standard Fourier
17 Shell Correlation of 0.143 (**Fig. 1d**). Local resolutions were estimated using BlocRes ²⁹.
18 Reconstruction statistics is listed in **Table S1**.

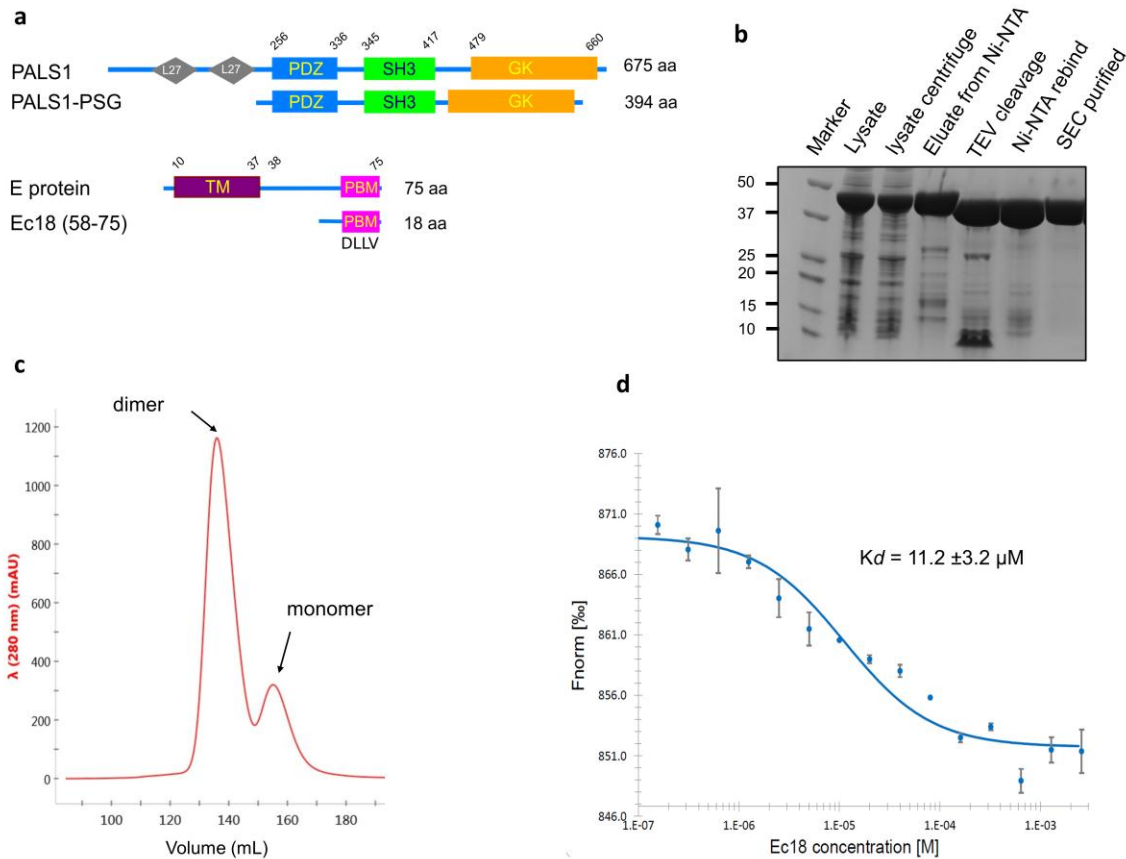
19 20 **Model building and refinement**

21 To assist our model building and refinement, we sharpened the masked and filtered map using
22 PHENIX ³⁰ with a B factor of -100 Å². We used the PDB code 4WSI as a starting model and built
23 the model for PSG and Ec18 in COOT ³¹ and refined the model iteratively using PHENIX. The
24 refined model was validated using Molprobtity ³² and the refinement statistics is listed in **Table S1**.

25 26 **Microscope thermophoresis (MST) measurement**

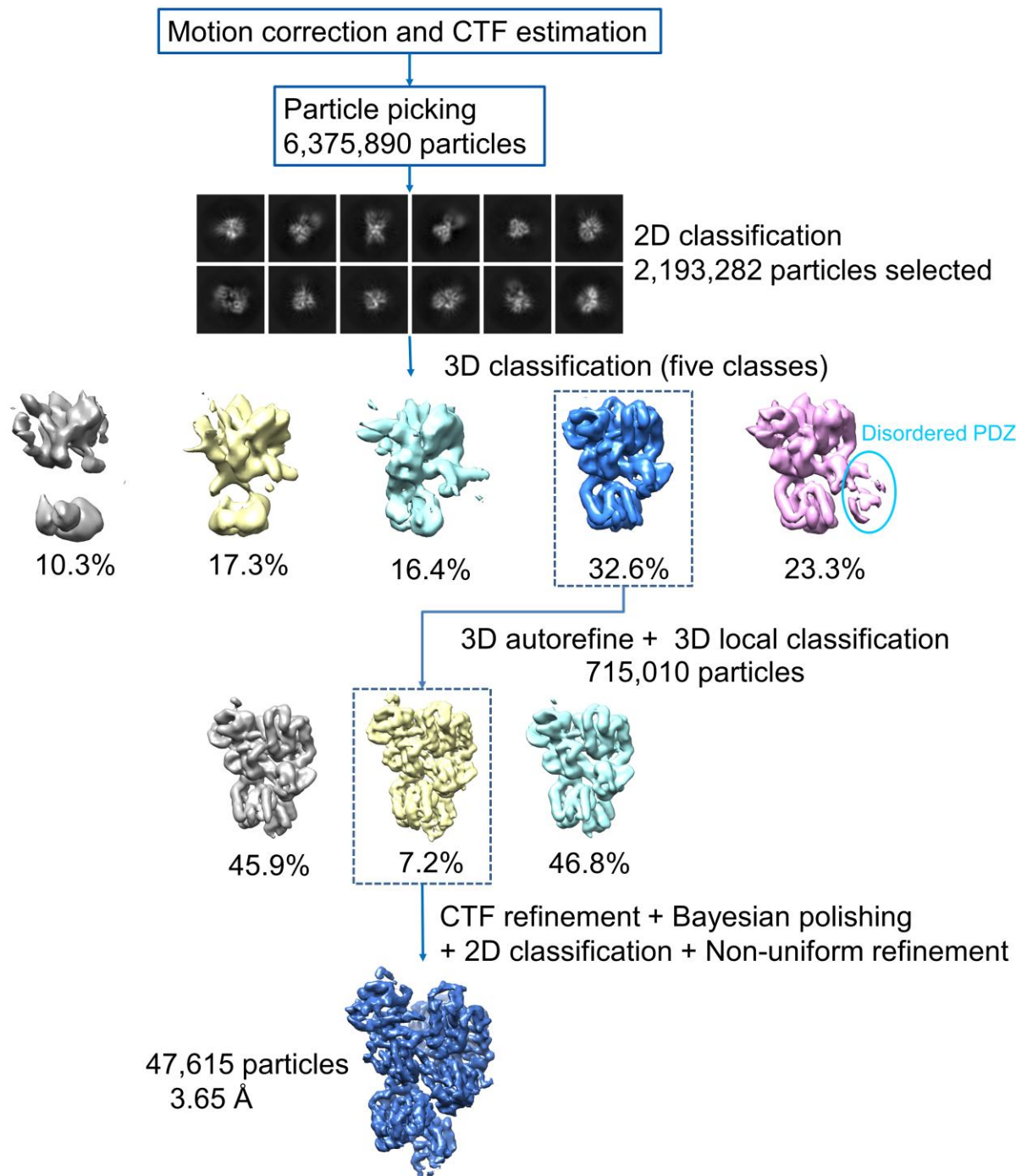
27 The binding affinity between Ec18 and PALS1-PSG was measured using a Monolith NT.115
28 instrument (Nanotempertech). Purified protein was buffer exchanged and covalently labeled
29 using dye NT647 following manufacture's protocol. The labeled protein was diluted 10x prior to
30 measurement in assay buffer containing 50 mM Tris, pH 7.5, 100 mM NaCl, 1 mM DTT, 1 mM
31 EDTA, and 0.05% Tween 20. Ec18 was dissolved in the assay buffer to a final concentration of
32 5.0 mM. Ten microliters of Ec18 was diluted 1:1 serially in the assay buffer and mixed with an
33 equal volume of labeled PSG. The PSG-Ec18 samples were incubated for 10min in dark at
34 room temperature before MST measurements. For all MST measurements, we used a MST

1 power medium, laser power 40%, and MST time 30 sec. NanoTemper program MO.Affinity
2 Analysis (Nanotempertech) was used for data analysis and curve fitting with a K_d model.



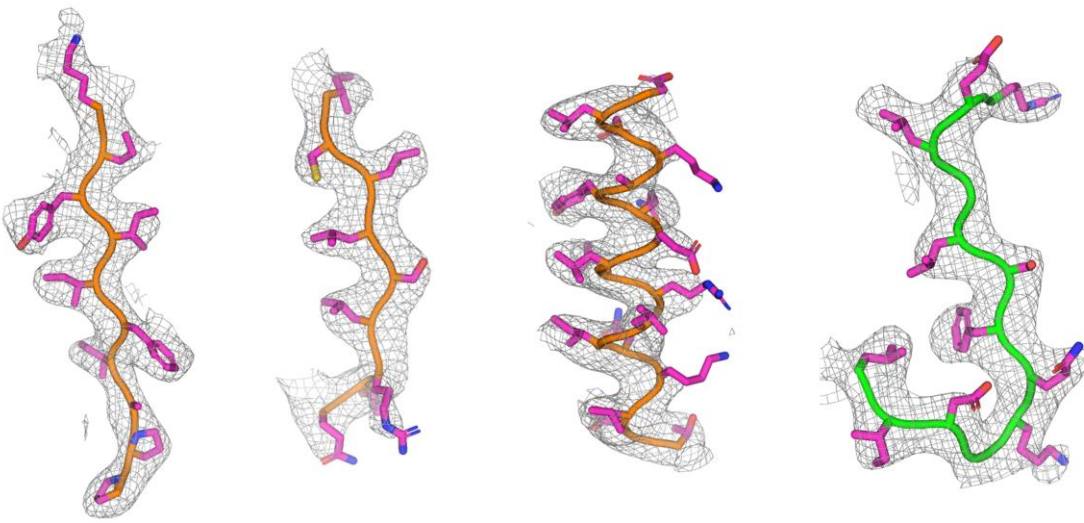
3

4 **Extended Data Fig. 1. Protein production.** (a) Schematics of the domains in PALS1 and E.
5 PALS1-PSG and Ec18 were used in this work. (b) SDS-PAGE analysis for the purification of PSG.
6 (c) SEC analysis for the purification of the PSG dimer. (d) Interactions between PALS1-PSG and
7 Ec18 measured by microscale thermophoresis (MST). PALS1-PSG was labeled by a
8 fluorescence dye NT-647 and was titrated using Ec18 at different concentrations. The fitted K_d is
9 $11.2 \pm 3.2 \mu\text{M}$. The error bar is the standard deviation from experiments of two different samples.



1

2 **Extended Data Fig. 2. A data analysis workflow.**



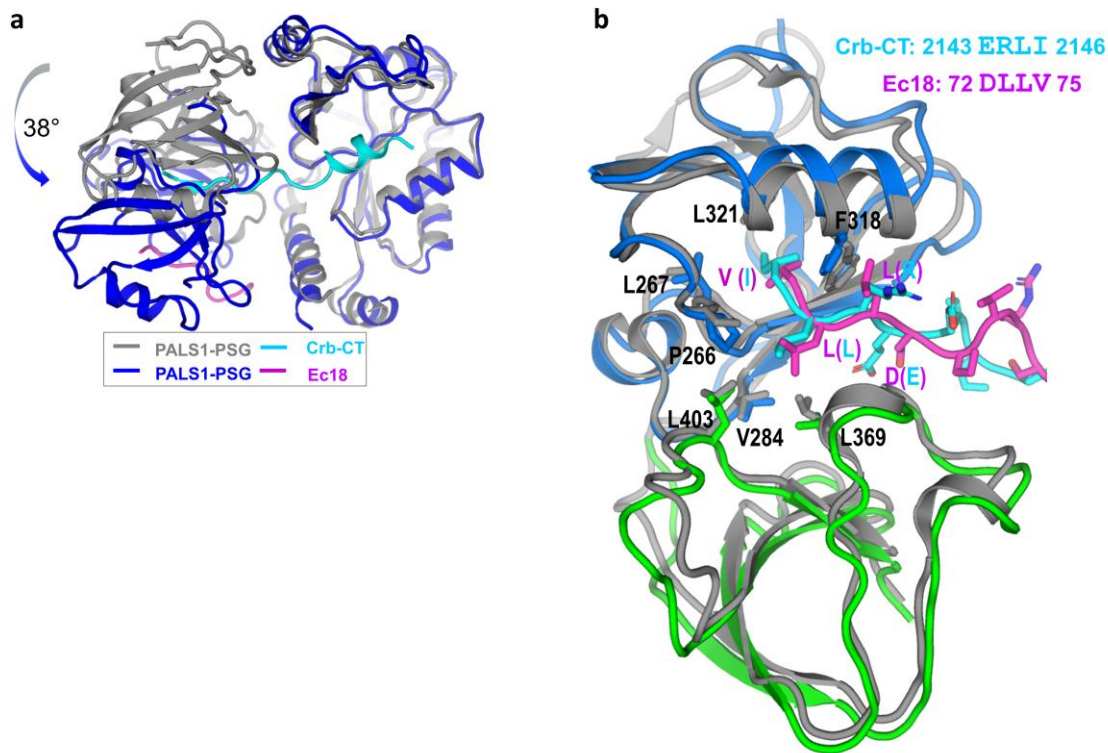
1

2

Extended Data Fig. 3. Quality of densities showing secondary structures and side chains.

3

4



1
2
3
4
5
6

Extended Data Fig. 4. Structural comparison of PSG-Ec18 with PSG-Crb-CT (PDB code 4WSI). (a) Alignment of the two complex structures based on the GK domain showing a relative rotation of about 38° for the SH3-PDZ domain. (b) Structural superposition for the SH3 and PDZ domains showing the binding sites for Ec18 and Crb-CT.

1 **Extended Data Table 1. Cryo-EM data collection, 3D reconstruction, and refinement**
2 **statistics.**

3

Data Collection

Microscope	Titan Krios G3i
Stage type	Autoloader
Voltage (kV)	300
Detector	Gatan K3
Energy filter (eV)	20
Acquisition mode	Super-resolution
Physical pixel size (Å)	0.684
Defocus range (µm)	0.7-2.5
Electron exposure (e ⁻ /Å ²)	64

Reconstruction

Software	Relion v3.08, CryoSPARC v2.15
Particles picked	6,375,890
Particles final	47,615
Extraction box size (pixels)	256
Rescaled box size (pixels)	64
Final pixel size	0.684
Map resolution (Å)	3.65
Map sharpening B-factor (Å ²)	100

model refinement

Software	PHENIX
Refinement algorithm	Real Space
Clipped box size (pixels)	None
Number of residues	627

R.m.s deviations

Bond length (Å) 0.007

Bond angle (°) 0.774

Molprobit clashscore 9.04

Rotamer outliers (%) 0.0

C β deviations (%) 0.0

Ramachandran plot

Favored (%) 85.65

Allowed (%) 14.35

Outliers (%) 0

PDB code XXXX
